The Journal of Chemical Physics

RESEARCH ARTICLE | JANUARY 27 2026

# Computational design of a ferroelectric framework material based on dipolar rotors

Thomas Bergler ; Sabuhi Badalov ; Achim Wixforth ; Dirk Volkmer ; Harald Oberhofer



*J. Chem. Phys.* 164, 044125 (2026)
https://doi.org/10.1063/5.0307483









AIP Publishing

The Journal of Chemical Physics ARTICLE pubs.aip.org/aip/jcp

# Computational design of a ferroelectric framework material based on dipolar rotors

Cite as: J. Chem. Phys. 164, 044125 (2026); doi: 10.1063/5.0307483
Submitted: 16 October 2025 • Accepted: 30 December 2025 •
Published Online: 27 January 2026



Thomas Bergler,[1] Sabuhi Badalov,[1] Achim Wixforth,[2] Dirk Volkmer,[3] and Harald Oberhofer[1,a)]

## AFFILIATIONS

[1] Chair for Theoretical Physics VII and Bavarian Center of Battery Technologies, University of Bayreuth, Universitätsstr. 30, 95447 Bayreuth, Germany
[2] Chair for Experimental Physics I, Member of Augsburg Centre for Innovative Technologies (ACIT), University of Augsburg, Universitätsstr. 1, 86159 Augsburg, Germany
[3] Chair of Solid State and Materials Chemistry, University of Augsburg, Institute of Physics, Universitätsstr. 1, 86159 Augsburg, Germany

[a)] **Author to whom correspondence should be addressed:** harald.oberhofer@uni-bayreuth.de

## ABSTRACT

In this work, we present a hierarchical approach to generate ferroelectric covalent frameworks based on rotatable polar groups. By using a multi-step workflow of increasing theoretical sophistication but also increasing computational costs, a unit cell with ferroelectric behavior can be generated for a given organic linker group. Starting with a basic point dipole model to find an appropriate unit cell, followed by a three-dimensional representation of the organic rotor, up to the full framework, each step confirms the desired attributes. This is achieved by using molecular dynamics and Monte Carlo Metropolis sampling in combination with the "Universal Force Field for Metall-Organic-Frameworks" (*UFF4MOF*) and the van der Waals corrected density functional tight-binding approach (known as GFN1-xTB) for the energy calculations. As a result, we demonstrate a covalent organic framework that is predicted to show a ferroelectric ground state that is stable up to temperatures beyond 100 K.





## I. INTRODUCTION

Covalent organic or metal-organic framework materials are known for their versatility in terms of possible functions and properties.[1,2] They can be synthesized to either be dense or yield wide-open pores; they can be functionalized for sensing,[3,4] storage,[5,6] catalysis,[7,8] or transport of ions[9] and—in some cases—also electrons.[10–12] This versatility is mostly due to the wealth of potential molecular level modifications that the linking units can undergo. Very recently, it has been shown that it is even possible to synthesize linkers that incorporate rotatable dipolar groups,[13,14] essentially making the framework material a polable dielectric. In all iterations to date, these rotors aligned randomly or antiferroelectrically at practically relevant temperatures,[15–17] yielding no net cell polarization, i.e., macroscopic ferroelectric poling. For various applications, like data storage,[18,19] enhanced active and tunable filters for gases and light,[20,21] and nanorotators[22–24] such 3D lattice mounted crystalline rotors might be utilized as highly parallelized molecular machines. A ferroelectric framework material would be a great advantage but has—not to date—been achieved. Part of this is due to the fact that, in contrast to inorganic ferroelectric materials, there is little to no theoretical guidance on how ferroelectric covalent organic or metal-organic framework materials based on rotatable groups could be designed. For example, there is no analytically solvable equivalent to a 3D Ising or Potts model for general lattices with dipoles rotating around arbitary aligned axes. In contrast, there have been efforts to design ferroelectric MOFs relying on the synthesis of structurally ordered dipolar linkers,[25] guided by computer simulations. The resulting overall dipolar MOF would then show an electric field gradient throughout a whole grain and, therefore, a vanishing overall energy gap between HOMO and LUMO. Such MOFs which, according to Nascimbeni and co-workers, may be hard to practically realize,[25] would only show a static ferroelectric ordering that could not easily be switched without breaking the framework itself.

Remanent polarization in a coordination framework compound, i.e., Rochelle salt, was already reported in the early 1920s.[26] Since then, a number of excellent reviews have been published on this topic,[27,28] highlighting that for ferroelectricity to occur, the material needs to contain a non-centrosymmetric polar point group. On the other hand, piezoelectricity in (metal-free) covalent organic frameworks (COFs) has a rather short history, owing to the common difficulties in obtaining highly crystalline COF materials.[29–34] The first examples of two-dimensional (2D) covalent organic frameworks functionalized with fluorinated alkyl chains have been reported very recently, showing robust switchable polarization.[30] The possibility to induce remanent polarization in framework compounds holding (dipolar) rotors as part of the framework was only suggested by Comotti and co-workers in 2016.[35] Overall design criteria and potential applications of 2D and 3D periodic compounds containing framework-mounted rotors have been the subject of a few recent reviews.[23,36,37] However, to the best of our knowledge, there exists as yet no report on a 3D periodic framework compound (either COF or MOF) in which a structural phase transition of framework-mounted dipolar rotors was unequivocally demonstrated, leading to spontaneous ferroelectric ordering, i.e., showing remanent dielectric polarization. This stands in sharp contrast to the many reports demonstrating ferroelectric phase transitions of polar guests hosted in the voids of porous coordination compounds, such as metal formate frameworks, for instance.[38] The lack of experimental evidence for the existence of such a kind of ferroelectric framework material might appear surprising at first glance; however, as we will show in the following, the reasons for this are manifold. Apart from symmetry requirements for producing ferroelectric ordered arrays of framework-mounted dipolar rotors, the subtle interplay between through-space, wide-ranging (collective) Coulombic and dispersive interactions, correlated with (strictly local) electronic rotation barriers, renders the ad hoc design of this type of ferroelectric framework material a complex task. In order to reduce the influence of the electronic rotation barrier for rotors mounted between two axles, most organic linker designs are going to fail, owing to very high rotational barriers that exceed the average non-covalent interactions between dipolar rotors by (at least) one order of magnitude. Recent examples in which rotational barriers have been minimized by appropriate linker design have led to a framework compound showing rotor dynamics down to very low temperatures (down to 2 K).[14] However, there is no evidence for a ferroelectric phase transition in these materials. Our own experimental investigations on MOFs containing linkers with framework-mounted rotors provided some hints at a possible phase transition upon antipolar ordering of dipolar rotors in a metal-organic framework,[16] but they failed with respect to emergent ferroelectric ordering. The difficulties noticed during this development provided further impetus for us to develop theoretical and retrosynthetic approaches that could ultimately pave the way toward a rational design of ferroelectric framework materials.

Therefore, in this work, we present a hierarchical numeric approach to solve the design problem of 3 dimensionally aligned rotating groups. Using various levels of abstraction, we uncover how different contributions to the total energy—ranging from the pure dipole, via more complex electrostatics, to non-electrostatic contributions such as van der Waals attraction and Pauli repulsion—influence the final alignment of the rotors. Finally, we present a prototypic framework (cf. Fig. 1) that, according to simulations, should show a ferroelectric phase at finite temperatures.

## II. METHODS SECTION

Monte Carlo and molecular dynamics simulations were performed using in-house Python-based codes integrated with the Atomic Simulation Environment (*ASE*).[39] Force fields and extended tight-binding energetics were computed with *LAMMPS*[40] and *CP2K*,[41] respectively. The *bonding topologies* for these simulations were generated using *LAMMPS-INTERFACE*.[42,43] Density functional theory calculations, including band structure analysis, were performed using the Vienna Ab initio Simulation Package (VASP) employing the projector-augmented wave method.[44–46] The Perdew–Burke–Ernzerhof (PBE) generalized gradient approximation (GGA) functional was utilized, with dispersion corrections implemented via the DFT-D3 approach employing Becke–Johnson damping.[47] A plane-wave cutoff energy of 520 eV ensured convergence. Electronic convergence criteria required energy differences between successive iterations to fall below $10^{-6}$ eV. Ionic positions were optimized until total forces on atoms within the unit cell were minimized to less than $10^{-5}$ eV/Å. Brillouin zone integrations were performed using Gamma-centered Monkhorst–Pack k-point meshes individually optimized to dimensions of $6 \times 6 \times 3$, $12 \times 12 \times 6$, and $6 \times 6 \times 6$ for the FE–COF–1 stator, FE–COF–2 stator, and the full FE–COF–2 framework, respectively. To obtain a reliable quantitative band structure, we used the HSE06 hybrid functional.[48]

### A. Cell generation

All our cells were generated in Python using the *ASE*library. For *set* 1, we restricted cells to a single rotor per unit cell and only varied the rotational axis and cell vectors under the restriction of a total cell volume of 1 $Nm^3$. For *set* 2, we randomly generated single-rotor structures based on the 13 Bravais lattices implemented in the *ASE*lattice package, which excludes the rhombohedral lattice for technical reasons. Using a hashing algorithm from the hashlib Python library, we ensured that the generated cells were unique to within machine precision. Using this approach, we generated 10 000 unique cells per dataset, which were then subjected to evaluation by Metropolis Monte Carlo.

### B. Selection of the rotor and rotor spacing

To achieve a high potential cell polarization, a rotor exhibiting a strongly dipole-like electrostatic potential was chosen [see Fig. 1(d) for comparison]. Here, we selected 2,1,3-benzoxadiazole, which in its molecular crystal structure already agglomerates in a permanent ferroelectric phase.[49] To find the optimal distance for these rotors, two energy-distance scans were performed with *xTB1-D3* in the *ORCA*[50] code. In addition, the non-bonding total energy was calculated for different distances and split into its main contributions, i.e., the Coulomb energy and van der Waals energy. For *xTB1-D3*, this means that the non-bonding total energy is the total energy of a boda rotor dimer minus twice the total energy of a boda rotor monomer (without dispersion energy). Then the Coulomb energy is the non-bonding total energy minus the dispersion energy of the

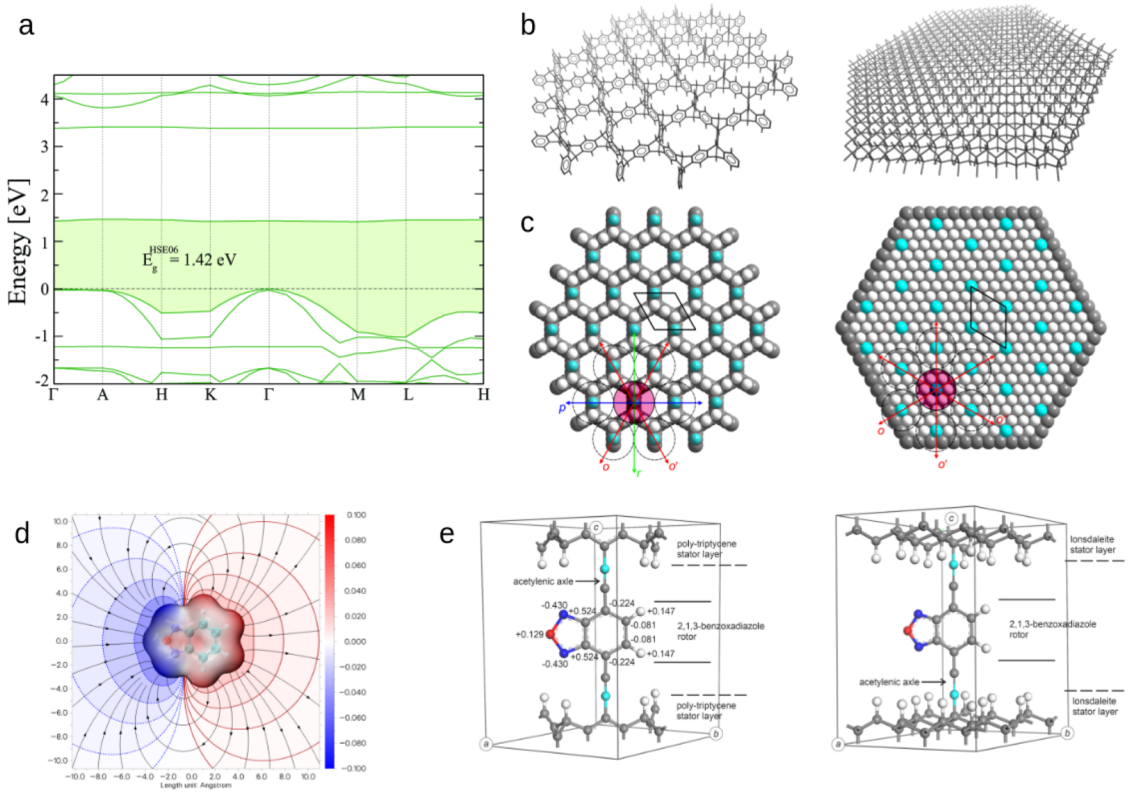


**FIG. 1.** (a) Band plot of the COF full FE–COF–2 calculated by VASP at the *HSE06* level with D3 correction-Becke–Johnson damping as vdW correction. (b) Left: The stator part of FE–COF–1: a single polytriptycene stator layer of FE-COF-1 generated in a hexagonal cell of lattice dimensions a = b = 8.89 Å, based on 2D condensed triptycene monomers, shown as a stick model in perspective view. Right: The stator part of FE–COF–2: a single polytriptycene stator layer of FE-COF-1 generated in a hexagonal cell of lattice dimensions a = b = 8.88 A, based on 2D condensed triptycene monomers, shown as a stick model in perspective view. It consists of a double-layer of sp-C-atoms based on the hexagonal diamante-polymorph *Lonsdaleite*. This lattice incorporates a higher symmetry for a 2D-layer than a normal cubic diamante lattice, which would feature offsets in the rotors in the z-direction. (c) CPK model for a poly-triptycene stator layer in top view (C, gray; H, white). H positions highlighted in cyan color indicate mounting points for rotor axles. Their distances are defined by the dimension of the hexagonal wallpaper group, shown as a black outline. The circle lines show the hexagonal dense packing arrangement of rotors, defining the size limit for pivoting rotors (~4.5 Å). The color lines indicate the six directions at which the closest possible head-to-tail arrangement will occur. Note that these are non-equivalent: the blue line indicates the two directions perpendicular (p) to the planar benzene moiety holding the acetylenic axle. The red lines indicate the four symmetry-equivalent oblique (o, o′, o″) directions. Left: The backbone of FE–COF–1 (P6mm, a = b = 8.989 252 Å). Right: The backbone of FE–COF–2 (P6mm, a = b = 8.806 900 Å). (d) ESP plot of 2,1,3-benzoxadiazole obtained from an electron density distribution analysis of a DFT calculation (B3-LYP, def2-TZVPP basis set). Color-coded 2D-ESP map of the electrostatic potential values within the symmetry plane of 2,1,3-benzoxadiazole (red and blue lines: ESP isocontour lines and black lines: ESP gradient corresponding to electric field lines). (e) Left: Unit cell of the primitive unit cell of FE–COF–1 (P1, a = b = 8.99 Å, c = 13.85 Å; $\alpha = \beta = 90°$; $\gamma = 120°$) showing a dipolar rotor mounted between poly-triptycene stator layers. Number labels show ESP-derived partial atomic charges assigned to the atom centers of a 2,1,3-benzoxadiazole rotor unit employed in force-field simulations. (No charge values were assigned to the atoms comprising the axles or the stator, respectively.) Right: Unit cell of the primitive unit cell of FE–COF–1 (P1, a = b = 8.81 Å, c = 13.78 Å; $\alpha = \beta = 90°$; $\gamma = 120°$) showing a dipolar rotor mounted between lonsdaleite stator layers.

dimer system. The van der Waals contribution is simply the dispersion energy of the dimer structure. The results can be seen in Fig. 2. They feature an energy minimum for the anti-parallel configuration at a distance of about 4 Å and a minimum for the parallel configuration at about 8 Å, which is mostly due to the Coulomb interaction between the two rotors in the FE configuration.

As the goal was to create COFs of high ferroelectricity, we designed our structures to favor parallel configurations. Consequently, we selected a rotor spacing of 8.81 Å, energy minimum for a head-to-tail arrangement of boda molecules. For the mounting of the rotor, two options were considered: a benzene unit featuring a $C_2$-symmetry or $sp^3$-bridgehead atoms of the stator featuring a $C_3$-symmetry. The first one would create a hexagonal closed packing of the rotors, while the latter would create a simple trigonal packing, resulting in steric limitations of the free rotations of the boda rotors. As the key point of this work is the free rotation of the rotors, the first mounting point was chosen.

### C. Generation of the COF

With the rotor alignment and distance selected, it was necessary to find a fitting backbone to connect the rotors. According to

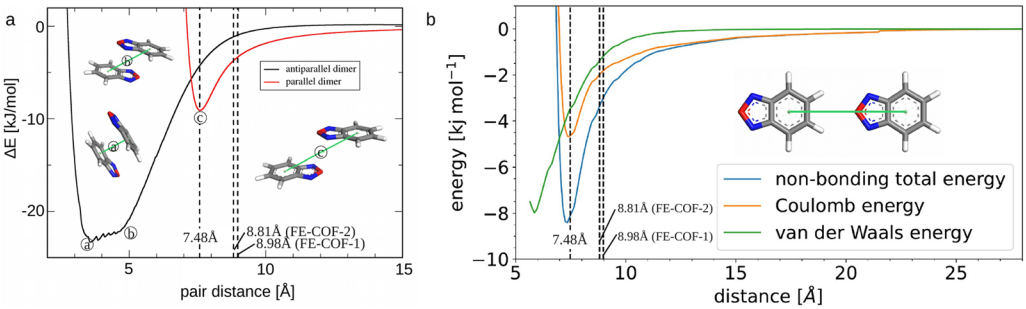


**FIG. 2.** (a) Calculation of the energetic stability of a FE- and an AFE-phase of the rotor depending on the distance between two rotors based on *xTB1-D3* calculations. (b) Calculation of the energetic contributions of the rotor in the FE-phase, depending on the distance between two rotors, based on *xTB1-D3* calculations.

our point-dipolar sampling, a hexagonal lattice energetically benefits FE phases; therefore, the honeycomb 2D backbone shown in Fig. 1(b) was chosen. Due to these stators, the acetylenic axels of the boda rotors are anchored to the $sp^2$-hybridized atoms in FE-COF-1 featuring an intrinsic rotational barrier of 16 kJ $mol^{-1}$, whereas in FE-COF-2 the rotor axes are bound to $sp^3$-hybridized C-atoms featuring an intrinsic rotational barrier of 0.2 kJ $mol^{-1}$. Note that the layer stacking in our compounds is of AAA type, i.e., all rotor axles are oriented on a common line in c-direction. We checked if an ABAB stacking of layers would change the behavior of the COFs. Yet, we found that the backbones sufficiently decouple the rotor layers such that no energetic difference between columnar and ABAB arrangements could be discerned. To make sure the stators of the rotors [see Fig. 1(e)] are not metallic, their bandgaps were checked. This was performed for the stator of FE–COF–1, the stator of FE–COF–2, and the full FE–COF–2. The results (see the supplementary material) indicate that none of the structures are metallic and, therefore, do not affect the FE phase of the COFs.

### D. Advantages and disadvantages of the FE–COF–2 structure

FE–COF–2 shows a much smaller intrinsic rotational barrier compared to FE–COF–1, which makes it much more applicable for ferroelectric materials as it is. However, the backbone of FE–COF–1 could achieve an even lower intrinsic rotational barrier of way below 0.5 kJ $mol^{-1}$ when the rotors are mounted to the $sp^3$-bridgehead atoms. However, mounting the rotors to the $sp^3$-bridgehead atoms of the stator of FE–COF–1 would not yield a hexagonal closed packed structure, which could negatively impact the formation of a FE phase. An improvement for FE–COF–2 could be a non-parallel stacking of the layers along the c-vector. An offset between each layer (creating an AB-layer structure) could positively influence the energies of the FE-phase (analogous to cholesteric liquid crystals). However, *xTB1-D3* calculations show that this is not the case (see the supplementary material).

### E. Monte Carlo of the point dipole representation of the rotor

Our lowest-level simulations were performed using a simple point dipole model with fixed rotational axes (cf. Fig. 3). The energy of each configuration was computed analytically as a sum over all pairs of dipoles $\vec{p}_i, \vec{p}_j$ using

$$E_{ij} = -\frac{1}{4\pi\varepsilon_0 r_{ij}^3}\left(\vec{p}_i \cdot \vec{p}_j - 3(\vec{p}_i \cdot \hat{\vec{r}}_{ji})(\hat{\vec{r}}_{ji} \cdot \vec{p}_j)\right), \quad (1)$$

where $\varepsilon_0$ is the vacuum permittivity, $\hat{\vec{r}}_{ji}$ denotes the normalized distance vector between dipoles, and $r_{ji}$ is its length. Due to the fact that dipole interactions decay with the third power of the distance, we implemented a distance cutoff of half the box-length, and periodic boundary conditions were applied via the nearest image convention. Dipole alignments were sampled using a standard Metropolis Monte Carlo scheme, where dipoles were selected randomly and rotated around their axis by a random amount. Maximum rotations were set such that the acceptance ratio was roughly 60%. For each temperature and simulation cell, we then sampled a total of 500 000

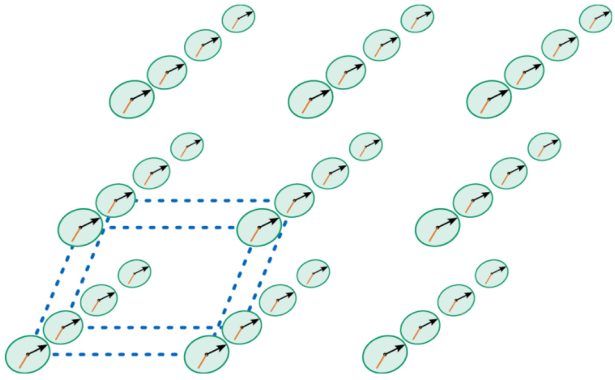

**FIG. 3.** Point dipole representation of the linker model used for the Monte Carlo simulations.

configurations, which showed a good enough preliminary convergence of the total dipole moment of the cell to distinguish between cells with ferroelectric phases and those without. For promising candidates, we followed this up with a longer MC sampling of $5 \times 10^6$ steps in total.

### F. Monte Carlo of the 3D representation of the rotor

To further test the results of the point dipoles, Monte Carlo simulations with three-dimensional rotors were performed. To do this, the 3D representation of the linker was placed in the identical cell as the point dipole and rotated such that the rotational axes align. Next, a $5 \times 3 \times 2$ supercell of this configuration was created so that a Lennard-Jones cutoff of 12.5 Å could be used to capture interactions between cells. In addition, every linker was rotated uniformly and randomly to ensure that the MC does not start in an energetically preferred state. After that, the program *LAMMPS-INTERFACE*[42,43] was used to generate the input and data files for *LAMMPS*.[40] Finally, the intrinsic rotational barrier that we have calculated with *xTB1-D3* in *ORCA*,[50] shown in Fig. 4, was manually added to the *LAMMPS* data files using an n-harmonic fit. With this setup, MC-runs were performed by uniform-randomly choosing one rotor and rotating it uniform-randomly between 1 and a maximum of 359°, calculating the configurations' energy with *LAMMPS*, and applying the Metropolis criterion on this energy. To achieve a target acceptance of 50%, the maximum step size was decreased during the run if needed. As this was not achievable for the very low temperatures (such as 0.1 K), we still achieved convergence by increasing the order of magnitude of total performed MC steps. Otherwise, we performed up to 10 000 MC steps (depending on the acceptance rate) for each temperature to get a well converged total dipole moment. To rule out any starting point biases, each of these runs was repeated for ten different initial seeds at different initial configurations, and their results were averaged.

### G. Monte Carlo of the FE–COF–2

In the COF, the dipolar alignment is sampled analogously to the previous steps; however, only 1000 steps were performed in each run due to the much higher computation cost (see Table I). To this end, we first sampled the rotors on the force field level again with *LAMMPS*. Finally, we also confirmed these calculations using a van der Waals corrected density functional tight-binding approach (known as GFN1-xTB) developed by Grimme and co-workers.[51]

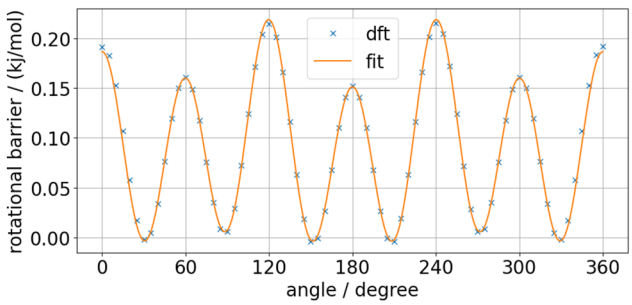


**FIG. 4.** Energetic rotational barrier of the linker model [cf. Fig. 1(e)] calculated by *xTB1-D3* with *ORCA* calculations used for the Monte Carlo simulations.

**TABLE I.** Computational costs for each method.

| Method | Cores/temperature | Core hours/step |
|---|---|---|
| Point dipole | 1 | $3.3 \times 10^{-8}$ |
| *UFF4MOF* MD | 56 | $4.5 \times 10^{-5}$ |
| *UFF4MOF* annealing MD | 56 | $3.8 \times 10^{-5}$ |
| *UFF4MOF* MC | 1 | $3.3 \times 10^{-5}$ |
| *xTB1-D3* MC | 128 | 2400 |

These simulations were performed using the *CP2K*[41] calculator for *ASE*.[39] A total charge of 0 was used, as the charges of the rotors were normalized and the charges of the backbone were set to zero, as an organic framework is charge-neutral and as their positions were fixed during the MC. Furthermore, a multiplicity of 1 was needed. For the van der Waals correction, *dftd3* was used. While for the xTB-parameters, *xTB1_parameters* were used. A periodic Poisson solver was used as the energy calculation was performed with periodic boundary conditions in all three directions. The AlphaxEwald parameter was set to 1.0, and the multigrid had a cutoff of about 280 Ry. To achieve a sufficient resolution, the SCF had a convergence level of $1.0 \times 10^{-6}$. For the Orbital Transformation (OT) method, the *DIIS* minimizer with the *FULL_S_INVERSE* preconditioner was used.

## III. RESULTS AND DISCUSSION

In our search for ferroelectric framework materials, we employ a multi-stage and multi-accuracy approach as outlined schematically in Fig. 5. This allows us to concentrate our computational resources on those materials that have a high probability of showing ferroelectric behavior. As a first step, we employ a computationally cheap model of point dipoles rotating around a fixed axis. Without analytic guidance for how such dipolar rotors should be distributed in a unit cell for optimal ferroelectric alignment, we first randomly generate 10 000 symmetry inequivalent unit cells (named *set* 1), with one rotor per cell and randomly oriented axes of rotation. To avoid physically infeasible structures and to better compare resulting structures, we impose a minimum distance between rotors and keep the overall cell volume constant while varying the cell vectors. Note that while the cells generated this way serve well as a first indicator of their feasibility as remanent ferroelectrics, they are mostly triclinic (space group P1) and, therefore, ill-suited for synthesis as a coordination network. Therefore, we also generated a second dataset of 10 000 inequivalent cells with higher symmetries, termed here the *set* 2. As a dipole moment for the rotors, we chose 0.852 eÅ (or 4.092 D),

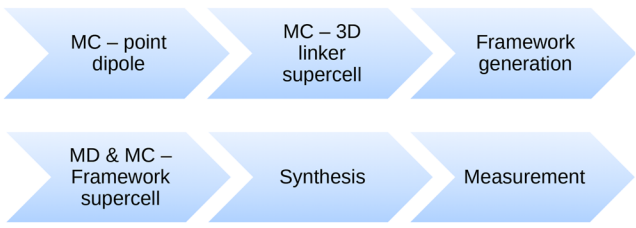


**FIG. 5.** Schematic of the workflow for the generation of ferroelectric frameworks.

which is the dipole moment of a benzoxadiazole (boda) rotor, which we also employ for our higher level atomistic studies below.

The resulting cells are then sampled using a Metropolis Monte Carlo scheme. By sampling each cell over a range of temperatures, we can assess their basic suitability as a ferroelectric. At the next level of complexity, we add atomistic detail to the rotors themselves. By fixing atomistic models of the benzoxadiazole rotor, we not only go beyond the highly simplified point-like representation of the dipole but also add—at the level of an analytic force field—non-electrostatic interactions between the rotors. To more realistically represent the situation of the rotor being part of a linker in a framework material, we also add, at this stage, a rotation potential computed from tight binding density functional theory.[51] Then, Monte Carlo sampling is again used to examine the alignment of dipolar rotors at various temperatures to confirm ferroelectric behavior. As a final test, the rotors are incorporated into a framework material to check for steric hindrances or dielectric screening that may potentially impede rotor alignment using the same methods. Finally, a Monte Carlo sampling at the tight binding density functional theory level is performed to verify the framework with quantum mechanical precision. In the following, we discuss this workflow in detail.

Each of these levels of theory comes at a vastly different computational cost. It would, for example, be quite impossible to perform our initial point dipole based screening of 10 000 structures at a quantum mechanical level, which makes our hierarchical approach all the more valuable. The computational costs associated with each level are given in Table I.

### A. Monte Carlo of the point dipoles

Using the analytic expression for the interaction between point dipoles, we perform Metropolis MC for each entry of *set* 1 at 50 K intervals between 1 and 701 K. Not surprisingly, we find that the majority of our cells do not show any appreciable polarization even at very low temperatures. Indeed, only 0.77% of the cells show an average polarization larger than half the possible maximum at 1 K, as depicted in Fig. 6. At room temperature, taken here as 301 K, this number shrinks to only 0.2%, or 20 cells.

All results are tagged with a unique ID and collected in a database, which is available for download at the Zenodo archive (cf. Data Availability Statement).

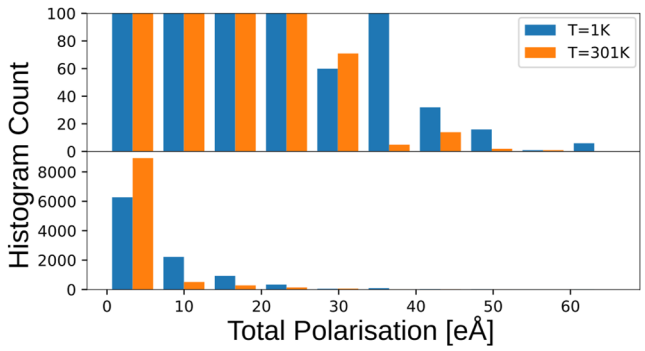


**FIG. 6.** Histograms of the average cell polarization at 1 K (blue) and 301 K (orange) of the *random* set. The top graph shows a zoomed-in image of the full histogram at the bottom.

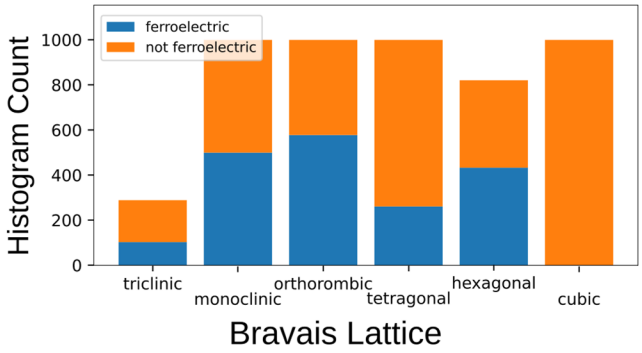


**FIG. 7.** Histograms of the cells showing ferroelectric ordering at 1 K for *set* 2, sorted by Bravais lattice type.

With a view to synthesizability, we then turn to *set* 2, where 10 000 single rotor cells were generated based on the Bravais lattice functionality implemented in the ASE Python package.[39] Similarly to *set* 1, these were subjected to evaluation by Metropolis MC. Again, we found the majority of cells did not show any ferroelectric ordering, even at 1 K. As depicted in Fig. 7, most cells again show no ferroelectric phase, with the strong ratios of ferroelectric to non-ferroelectric cells found for low symmetry tri- or monoclinic space groups which, as mentioned before, would not lend themselves easily to the construction of coordination frameworks. Even stronger ratios were found for orthorhombic and hexagonal space groups. Note that the break in symmetry necessary for ferroelectric ordering is provided by the dipolar rotors represented here through point dipoles. Based on the findings of the point dipole model, we subsequently consider two cells, both simplified versions of the hexagonal cell, yet with a rotation axis aligned with the z axis. The COFs associated with these cells are named FE–COF–1 and FE–COF–2 and are described in more detail in the methods section.

Finally, we note that the point dipole model can only serve as a very crude first guess for a number of reasons. First, omitting all interactions but dipole terms obviously is not a very realistic depiction of reality, as we demonstrate below. Second, due to the relatively small dipole moments and large distances involved, the overall interaction strengths tend to be rather small as well. This results in strongly fluctuating total dipole moments over the full temperature range, where ferroelectric and antiferroelectric orderings compete. This is illustrated in Fig. 2 of the supplementary material, which does show oscillatory behavior between the two orderings already at a temperature of 201 K.

### B. Monte Carlo of the 3D representation

As the next level of sophistication of our simulation, we created 3D models of the rotating groups to replace the point dipoles, yet with their rotation axes aligned. We again proceed to sample the phase space of these rotors with Metropolis MC at various temperatures. In order to rule out sampling issues, we perform the MC runs with ten different random seeds. The results for the cell of COF FE–COF–1 and FE–COF–2 are shown in Fig. 8, with the averaged results depicted in blue. For both cells, the total cell polarization is constant at the maximum value for temperatures below ~100 K,

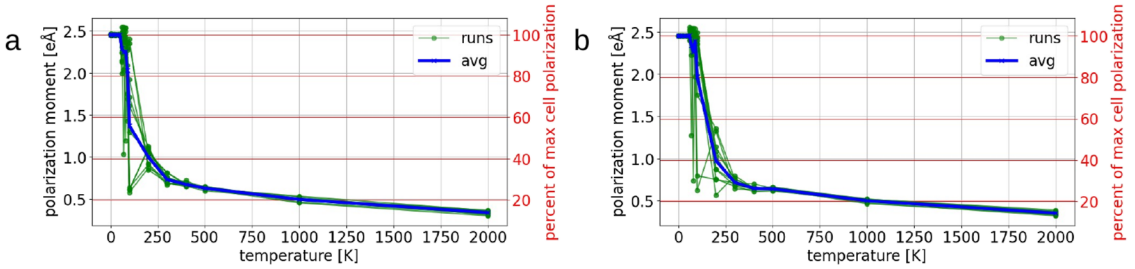


**FIG. 8.** Results of the 10 MC simulations of the 3D representation of the linkers in the cell of COF FE–COF–1 (a) and FE–COF–2 (b). Depicted are the polarization moment and its percentage in reference to a fully ferroelectric system. Shown are the ten runs with different starting seeds in green and the averaged value in blue.

indicating a ferroelectric phase. After 100 K, a steep drop in the polarization indicates a phase transition.

### C. Molecular dynamics of the 3D FE–COF–2 with *UFF4MOF*

Next, we implement the rotor configuration in a three dimensional COF to test its feasibility in a realistic setting. In order to first gauge the stability and steric limitations of the rotations of the rotors in a dynamical situation, a number of Molecular Dynamics (MD) simulations were performed. As described in the methods section, the rotational barrier calculated by *xTB1-D3* is about 0.2 kJ mol$^{-1}$, which is equivalent to a thermal energy of about 24 K. Therefore, one MD at 5 K, a little below that barrier, was performed to confirm that the barrier prevents rotations. Another MD at 50 K, a little above the rotational barrier, was performed to test the influence of the Coulomb and Lennard-Jones interactions upon the rotor rotations. In addition, finally, a third MD was performed at a high temperature of 500 K to overcome the barriers of all energetic contributions and only sample the steric limitations. We used *LAMMPS* and *UFF4MOF* for all MD runs at a runtime of $1 \times 10^6$ timesteps of 1.0 fs. The results are depicted in Fig. 9. It is important to note here that the polarization as the sum of the dipole moments was divided by a fixed reference configuration of maximum polarization of a perfect ferroelectric configuration in the reference cell. As the rotor geometries could not be fixed during the MDs, their bonds fluctuate

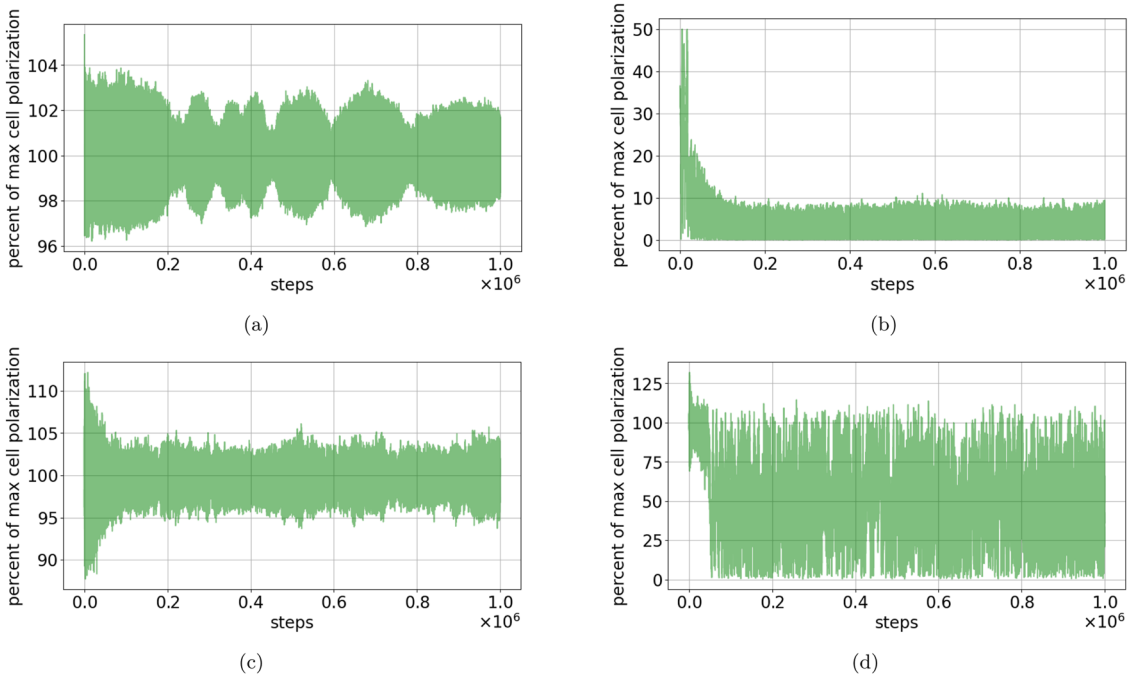


**FIG. 9.** MD of the FE–COF–2 at different temperatures for $1 \times 10^6$ steps. (a) 5 K-ferroelectric configuration. (b) 5 K-anti-ferroelectric configuration. (c) 50 K-ferroelectric configuration. (d) 500 K—neither FE nor AFE configuration.

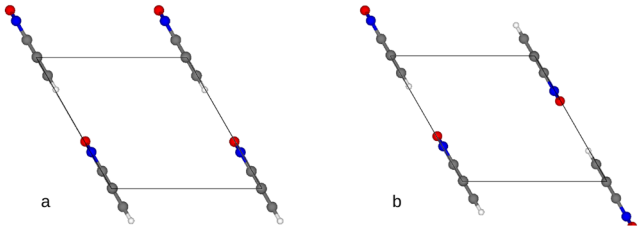


**FIG. 10.** Ferroelectric and anti-ferroelectric configurations of the FE–COF–2. Shown are only four rotors and the unit cell, excluding the backbone and linkers. (a) The ferroelectric configuration of the FE–COF–2: All rotors are parallel to each other. The rotors point at each other head-to-tail. (b) The anti-ferroelectric configuration of the FE–COF–2: Every line of rotors is antiparallel to each other. In every line, the rotors point at each other head-to-tail.

a little around their energetic minimum, resulting in a small compression or expansion of the rotor. This, in turn, then decreases or increases their dipole moment slightly. Therefore, even an MD of perfect ferroelectric rotations fluctuates around 100% of the identical but fixed reference system, such that values above 100% appear as artifacts. Obviously, these fluctuations increase with increasing temperature.

Figure 9(a) shows that for some random starting rotations at low temperatures, the polarization fluctuates around the maximum polarization possible for the FE–COF–2, i.e., with all rotors parallel to each other and pointing head-to-tail [see Fig. 10(a)]. Figure 9(b), on the other hand, shows that for other random starting rotations at low temperatures, the polarization fluctuates around zero, which in this case corresponds to all rotors aligning antiparallel to each other and pointing head-to-tail [see Fig. 10(b)]. Figure 9(c), however, shows that at a temperature above the rotational barrier, the polarization is still fixed to its maximum. Finally, Fig. 9(d) depicts the occurrence of all possible polarizations from 0% to 100% of their theoretical maximum at high temperatures.

Our MD calculations thus clearly show that at temperatures lower than the rotational barrier divided by Boltzmann's constant, no free rotations occur on the timescales observed, and only small fluctuations around either the ferro- or anti-ferroelectric minima are possible. At temperatures significantly higher than the barrier, rotations are still frustrated due to the large head-to-tail attraction of the rotors, which can only be overcome at much higher temperatures. (Anti-)ferroelectric behavior in these structures is thus a product of electrostatic and van der Waals interactions, not due to rotational barriers.

To understand the energy differences of the FE and AFE phases in more detail, we performed a geometry optimization at the *UFF4MOF* level, starting from the structures of minimal energy of both 5 K MDs. The resulting total energies of both optimized structures were calculated by *UFF4MOF* and split into their main contributions, i.e., the Coulomb energy, the van der Waals interaction, and the intrinsic rotational barrier. The latter is equal for both configurations, while both Coulomb and van der Waals energies are slightly lower for the ferroelectric case. The Coulomb energy is lower by 1 kJ mol$^{-1}$ (or 0.25 kJ mol$^{-1}$ per rotor), while the van der Waals contribution is lower by 2 kJ mol$^{-1}$ (or 0.5 kJ mol$^{-1}$ per rotor). Overall, the energy of the optimized ferroelectric phase is thus lower by 3 kJ mol$^{-1}$ (i.e., 0.75 kJ mol$^{-1}$ per rotor) compared to the energy of the optimized structure of the anti-ferroelectric phase, reinforcing our earlier MC results showing a pronounced ferroelectric phase at low temperatures. Note that due to the comparatively small energy difference between both phases, a correct choice of rotor attachment is of great importance. A rotor bound by a triple bond bound to two sp$^3$-C-atoms, such as the one used for FE–COF–2, shows an intrinsic rotational barrier of only 0.2 kJ mol$^{-1}$, much smaller than the energetic difference between the two phases. For comparison, the same rotor bound by a triple bond to sp$^2$-C-atoms and sp$^3$-C-atoms (as in FE–COF–1) would show a much greater intrinsic rotational barrier of about 16 kJ mol$^{-1}$ and, therefore, would be much greater than the energetic difference between the FE and AFE phases, most likely leading to a hindered rotation and preventing the system from adopting its ferroelectric state. This is the reason why we chose FE–COF–2 as our main model for further analysis. The sp$^3$-carbon linkage employed there to mount the rotors shows a very low intrinsic rotational barrier, whereas the initial FE–COF–1 rested on a mounting of the acetylenic axles to sp$^2$-C atom centers featuring a much higher barrier (cf. the methods section). Note, though, that a vanishing rotational barrier still does not guarantee the existence of a ferroelectric phase. On the contrary, one might postulate such a phase to form if the rotors are driven into parallel alignment by the rotation potential instead of other energetic contributions.

### D. Annealing molecular dynamics of the FE–COF–2 with *UFF4MOF*

Next, we ascertained whether the ferro- or anti-ferroelectric ordering is the thermodynamically more stable one at low temperatures. To this end, we again performed simulated annealing for the FE–COF–2 with MD based on *UFF4MOF* implemented in *LAMMPS*. At the start, the system was thermostatted at 500 K to ensure a completely free rotation of the rotors. This temperature was sampled for $1 \times 10^6$ steps before the temperature was decreased (by thermostat) to 100 K for another million steps to cross the energetic barrier of Coulomb and Lennard-Jones interactions. Finally, to cross the energetic intrinsic rotational barrier of the rotors, the temperature was decreased to 1 K for another million steps.

Figure 11(a) depicts the total polarization of the cell during each step, while Fig. 11(b) depicts the temperature profile of the MD during the course of the annealing process. Note that during the high temperature run, from 0 to $1 \times 10^6$ steps, the full possible range of the total dipole, from 0% to 100% of its maximum, appears. For the intermediate temperature, from $1 \times 10^6$ to $2 \times 10^6$ steps, the sampling of the full range of dipoles becomes less pronounced. Finally, in the low temperature phase, from $2 \times 10^6$ to $3 \times 10^6$ steps, the total cell dipole collapses to a stable ferroelectric configuration with 100% polarization.

### E. Monte Carlo of the FE–COF–2 with *UFF4MOF*

For a more detailed understanding of the temperature behavior of our 3D COF, we again turn to MC simulations in a $2 \times 2 \times 1$ supercell. The results of the 10 MC runs of this structure performed with *UFF4MOF* in *LAMMPS* are depicted in Fig. 12. One can see a constant polarization moment density for temperatures below about

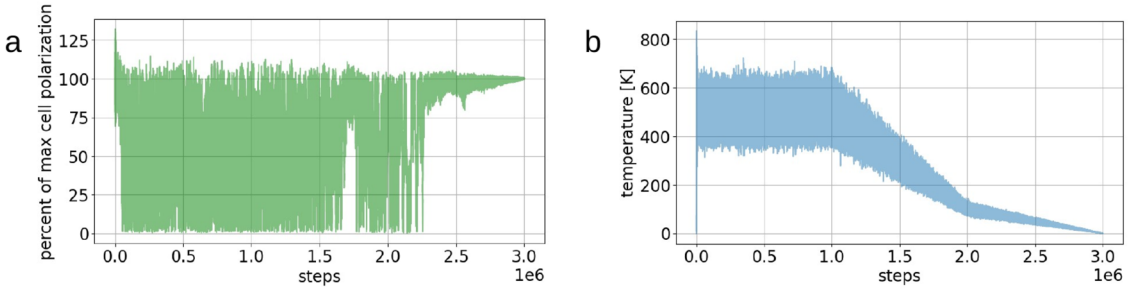


**FIG. 11.** Polarization moment (a) and instantaneous temperature (b) during the annealing MD of the FE–COF–2 using *LAMMPS* with *UFF4MOF*.

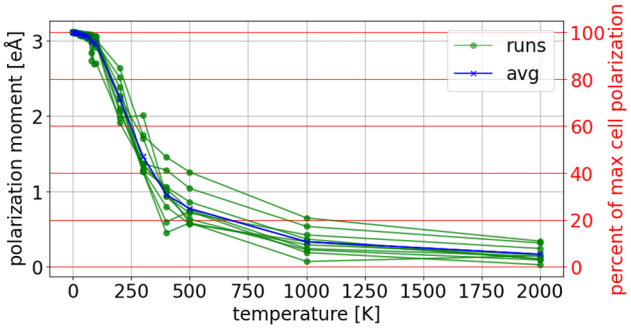


**FIG. 12.** Average values of the polarization taken from 10 MC simulations of the FE–COF–2. Depicted is the polarization moment as well as its percentage with reference to a fully ferroelectric system. Shown are the ten runs with different starting seeds in green and the averaged value in blue.

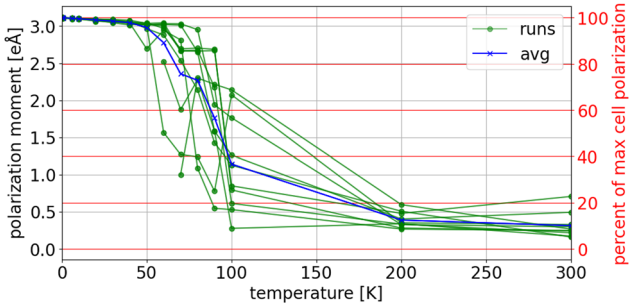


**FIG. 14.** Average values of the polarization of FE–COF–2 from MC simulations based on *xTB1-D3* energetics taken from 10 MC simulations of the FE–COF–2. Depicted is the polarization moment as well as its percentage with reference to a fully ferroelectric system. Shown are the different runs with different starting seeds in green and the averaged value in blue.

100 K. While for temperatures above 100 K, the cell's total polarization shows a steep drop.

The constant average total polarization for temperatures below roughly 100 K (cf. Fig. 12) indicates that the rotations of the linker of the FE–COF–2 are frustrated there. At temperatures above 100 K, a drop in the polarization moment indicates free rotations of the rotors and, therefore, a phase transition.

## F. Monte Carlo of the FE–COF–2 of different supercells

In order to test long range polarization and, therefore, possible finite size effects, we next performed MC simulations of different supercell sizes based on *UFF4MOF* energies. In particular, 2 × 2 × 2-, 3 × 3 × 3-, and 4 × 4 × 4-supercells were tested. The results are depicted in Fig. 13. For all supercell sizes, the polarization is con-

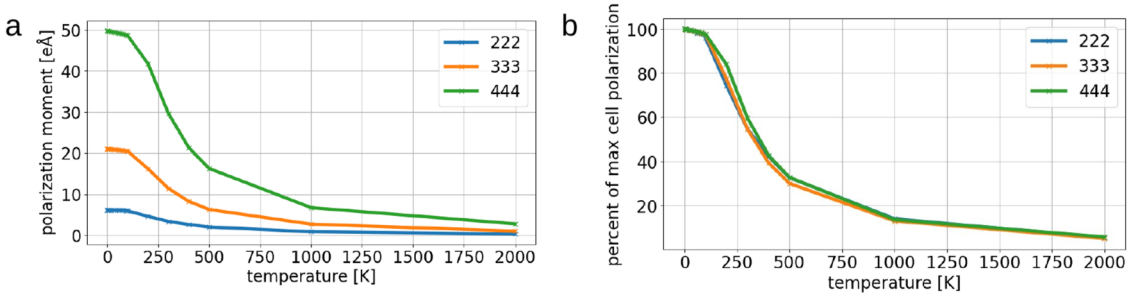


**FIG. 13.** Results of the MC simulations of the FE–COF–2 with *UFF4MOF*. Shown are the averaged results of 3 different supercells with ten runs of different starting seeds each. The supercells tested were 2 × 2 × 2, 3 × 3 × 3, and 4 × 4 × 4. (a) shows the absolute values of the polarization, while (b) depicts the values of the polarization as a percentage of the maximum possible polarization at the ferroelectric configuration.

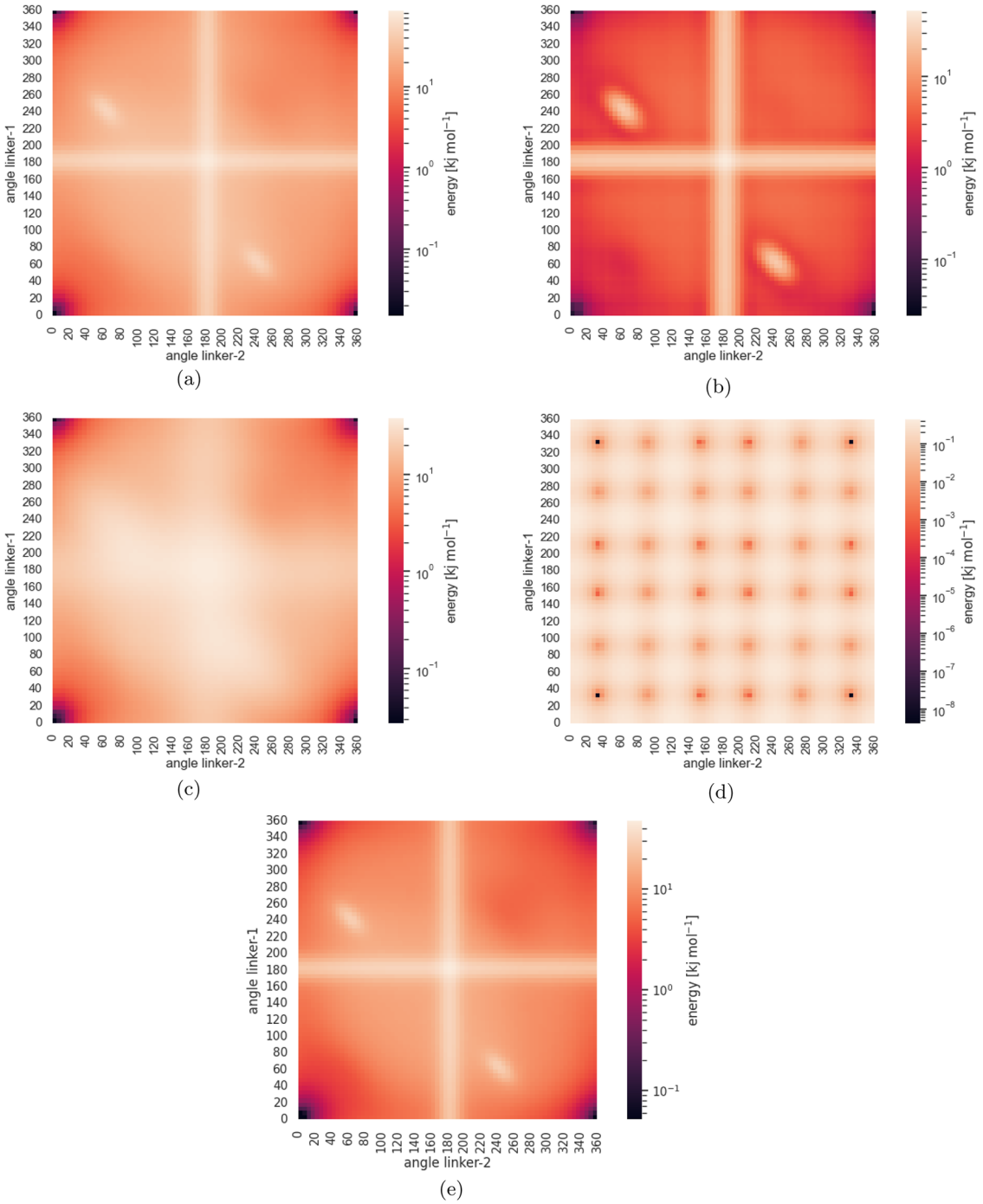


**FIG. 15.** Heatmaps of the results of the energy calculation for 5184 rotations of 5° steps of two linkers of the FE–COF–2 against each other, with all other linkers fixed in their optimal FE configuration. Note that darker colors depict energetically more favorable configurations. (a) Heatmap of the calculations with *UFF4MOF* in *LAMMPS* with Lennard-Jones interactions, Coulomb interactions, and the intrinsic rotational barrier active. (b) Heatmap of the calculations with *UFF4MOF* in *LAMMPS* with only Lennard–Jones repulsion interactions active. (c) Heatmap of the calculations with *UFF4MOF* in *LAMMPS* with only Coulomb interactions active. (d) Heatmap of the calculations with *UFF4MOF* in *LAMMPS* with only the intrinsic rotational barrier active. (e) Heatmap of the calculations with *xTB1-D3* in *CP2K*.

stant at its maximum at temperatures below about 100 K before it starts to slowly drop above this temperature.

While the different supercells, naturally, show different total polarizations, their relative polarization profiles [cf. Fig. 13(b)] coincide, thus ruling out any finite size effects.

### G. Monte Carlo of the FE–COF–2 with *xTB1-D3*

Finally, given the approximate nature of the *UFF4MOF* force field, we next turn to more rigorous energetics with *xTB1-D3* as implemented in *CP2K*. Note that, while this definitely represents an improvement, it still has its limitations compared to, e.g., hybrid density functional theory or coupled cluster theory.[52] Following the same procedure as before, we depict the resulting average cell polarizations at different temperatures in Fig. 14. In addition, here, we find the ground state to clearly be a ferroelectric one, yet the onset of the melting of the ferroelectric phase already starts much earlier, such that already above 80 K, the total polarization has dropped to only half of its maximum value.

### H. Contributions to the total rotational energy

So far, our results pointed toward FE–COF–2 showing a ferroelectric state at low temperatures. In order to quantitatively understand this behavior, we next separate the energy contributions in our force field calculations into electrostatics, Lennard-Jones terms, and the contributions from the rotational barrier. To illustrate these contributions, we map each of them for the full rotation of two neighboring linkers in a supercell with all other linkers fixed at the position of the ferroelectric total energy minimum. A similar map, but with all linkers rotating in unison, is given in Fig. 2 of the supplementary material. Rotational space was sampled in 5° steps for a smooth map. We compare each of the contributions to the full map and to the *xTB1-D3* energetics.

Considering the full results of all active contributions [Fig. 15(a)], we note two distinct peaks at the rotations 60°–230° and vice versa at 230°–60°. These are the configurations in which the two rotated linkers point at each other head-to-head [see Figs. 16(a) and 16(b)]. Furthermore, we find two "bands" at around 180°-x° as well as around y°-180°, forming the highest peak at 180°–180° at about 85 kJ mol$^{-1}$. For both of these bands, one of the benzoxadiazole rotors, respectively, points directly at one of the static rotors of the FE–COF–2 (one of the two linkers that was not rotated during this test), with 180°–180° being the configuration of both rotors pointing at their fixed neighbors [see Fig. 16(c)]. The origins of both those features can easily be spotted in the pure Lennard-Jones results depicted in Fig. 15(b) and the pure electrostatic map of Fig. 15(c). Both Lennard-Jones and Coulomb show the peaks and bands, yet the repulsive contributions of the Lennard-Jones potential are much more pronounced, with Lennard-Jones contributing around 50 kJ mol$^{-1}$ of 85 kJ mol$^{-1}$ to the central peak.

Considering the minima, we see that both electrostatics and Lennard-Jones interactions (and, therefore, also the full map) have a pronounced minimum for parallel ordering, shown as dark red spots in the corners of Figs. 15(b) and 15(c). This indicates that, at least in a single row, rotors favor a parallel ordering. This, together with the distinct peaks and bands, confirms our observations that in this COF, a direct antiferroelectric ordering with rotors pointing toward each other is energetically unfavorable. Indeed, the low temperature antiferroelectric phases we observed during the MD runs were composed of antiparallel layered bands of rotors.

Finally, the rotational barriers are depicted in Fig. 15(d) only for the sake of completeness. Given that for the triple bond employed to support the rotors, we had to specifically add a rotational potential term (cf. Sec. II), the rotational barrier heat map reproduces exactly this potential. The heatmap shows a lattice-like structure consisting of 6x6 peaks at a very small energy of about 0.40 kJ mol$^{-1}$, which again indicates the minor role played by the rotational potential compared to other energy terms. Indeed, the rotational potential would show a maximum at the perfectly aligned orientations, but this has no influence on the stable state.



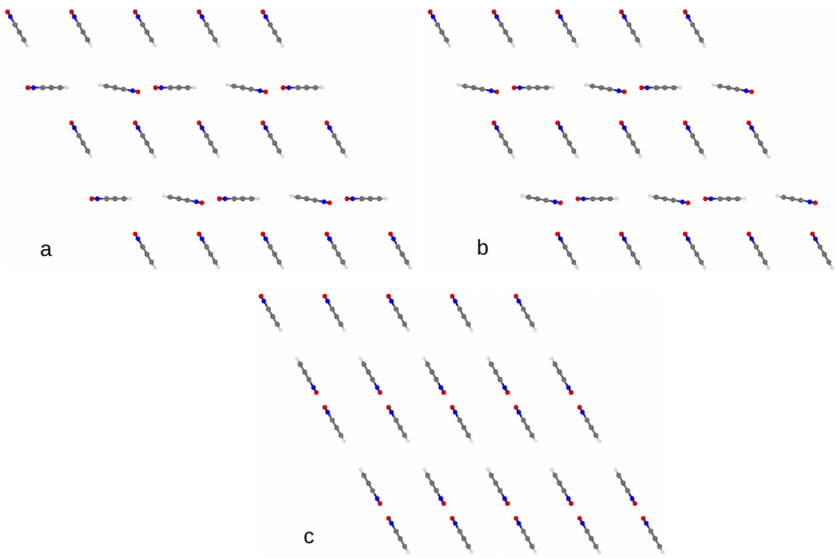


**FIG. 16.** Snapshots of the energetically unfavorable configurations of the 5184 rotations of 5° steps of two center linkers of FE–COF–2 against each other, used within the energy calculations of the heatmaps. (a) 60°–230° configuration—the two rotating center linkers point at each other's periodic images head-to-head. (b) 230°–60° configuration—the two rotating center linkers point at each other head-to-head inside the cell. (c) The 180°–180° configuration—the two rotating center linkers point at the remaining fixed linkers on the edges head-to-head.

In a quantum mechanical calculation, such as *xTB1-D3*, we cannot as easily decompose the energy terms, but we see that it shows broadly the same behavior as our force field calculations [cf. Fig. 15(e)]. This explains the observation that *xTB1-D3* calculations reproduce similar structures to the force field calculations. Note that the peaks we find in the *xTB1-D3* map are roughly half of the energies we found for *UFF4MOF*, which explains the lower melting point of the ferroelectric phase.

## IV. CONCLUSION

The aim of this work was to computationally generate a framework material that shows a remanent ferroelectric phase. In service to this goal, we developed a hierarchical screening approach allowing us to quickly weed out structures that do not lead to any ordered phases and concentrate on those that do, focusing computational resources on these promising candidates only. The workflow itself relies on successively adding complexity to the model, starting from a highly simplified point dipole model, progressing through an atomistic force-field model of rotors fixed in space, and culminating in an extended tight-binding DFT of a full framework material. This allowed us to screen 10 000 distinct structures for ferroelectricity. While the point dipole model's simplicity leads to quite noisy results, which sometimes fluctuate between ferro- and anti-ferroelectric ordering, it clearly highlighted those structures where no ordering occurs. The initial search of *set* 1 yielded a triclinic structure as an optimal choice for remanent ferroelectricity. Unfortunately, such low symmetry structures do not readily lend themselves to the generation of a coordination framework. We thus also screened another set (*set* 2) of 10 000 structures with higher symmetries to find a hexagonal grid that is most robust with regard to the formation of ferroelectric phases.

Based on these findings, we designed a COF named FE–COF–2 that does show a clear ferroelectric phase at low temperatures. Depending on the level of theory, this phase is predicted to persist up to between 100 and 200 K. Thereby, the lower temperature is predicted by the higher-level *xTB1-D3* approach. Our in-depth analysis of the energy contributions shows a mixture of Lennard–Jones and electrostatic interactions to be responsible for the ordering of the rotors, while rotational potentials play only a secondary role for a well-designed rotor. The vastly reduced intrinsic rotational barrier of FE–COF–2 compared to the earlier version, FE–COF–1, permits the Lennard–Jones and electrostatic interactions to play the major role in the dynamics and, therefore, enables the formation of ferroelectric phases. The energetics of the force field and tight binding DFT calculations fully agree in their overall features, leading to the existence of the ferroelectric phase in both levels of theory. Yet, the maxima and minima of the *xTB1-D3* are lowered by about a factor of 2 compared to *UFF4MOF*, which explains the lower melting temperature of the quantum mechanical calculations. Considering that *xTB1-D3* is also known to suffer from some errors,[53] future DFT calculations, potentially beyond the level of the standard generalized gradient approximation, would be needed to exactly determine the transition temperature.

Next to the ferroelectric phase, our molecular dynamics simulations also show the existence of an antiferroelectric phase where ordered bands of rotors align antiparallel to each other. An annealing molecular dynamics simulation starting from high temperatures, though, also shows that it is only the ferroelectric phase that forms once the phase transition temperature is reached. The ferroelectric phase was found to be lower in energy by about 0.75 kJ/mol per rotor compared to the antiferroelectric one. With a view to the future, perhaps even room-temperature-stable ferroelectric COFs, our results suggest some improvements. First, the electrostatic interaction could be strengthened by increasing the polarity of the rotors even further. Similarly, shorter distances between the rotors would increase both electrostatic and non-electrostatic interactions. Furthermore, a stronger alignment of rotors at high temperatures might be reached with a clever alignment of the rotation potential of each of the rotors. Yet, these would likely also benefit the anti-ferroelectric striped phase. Therefore, for a room temperature ferroelectric COF, there likely needs to be a balance between rotation potential, electrostatic, and dispersive interactions. This explains why no such coordination framework has been found to date but also shows how our analysis can point the way toward such materials.

All in all, we used a multi-stage approach to first demonstrate the feasibility of using polar rotors in a lattice to form remanent ferroelectric phases and found hexagonal Bravais lattices to yield the most robust ferroelectric high symmetry phases. Based on these insights, we generated a low temperature ferroelectric COF structure, which we studied on a force-field and extended tight-binding level to again reproduce their ferroelectricity.

## SUPPLEMENTARY MATERIAL

In the supplementary material, we show a deeper analysis of the point dipole data. We provide a rotational analysis of the energetics of the ferro- and anti-ferroelectric configurations of FE–COF–1 and FE–COF–2. Furthermore, we show that hydrostatic compression or expansion of the COF strengthens and weakens the ferroelectric phase, respectively. In addition, we show that the stacking order of the layers of FE–COF–2 (AA vs AB) does not influence the energetics of the rotors. Finally, we present the electronic band diagrams of the stators of both COFs and the band structure of the full FE–COF–2 to show that they are non-metallic in nature.

## ACKNOWLEDGMENTS

The authors are grateful for financial support from DFG Grant Nos. VO 829/12-2, WI 1091/20-2, and OB 425/3-2 (DFG Priority Program 1928 "Coordination Networks: Building Blocks for Functional Systems COORNETs"). HO and TB further acknowledge support from the "Solar Technologies go Hybrid" consortium, supported by the Bavarian Ministry of Science and Art. Computations were carried out on the HPC systems Festus (DFG Grant No. 523317330) of the University of Bayreuth. Furthermore, we wish to acknowledge the *multwfn* developer, **Tian**, for his quick support regarding the depiction of the COF's field lines.

## AUTHOR DECLARATIONS

### Conflict of Interest

The authors have no conflicts to disclose.

## Author Contributions

**Thomas Bergler**: Data curation (equal); Formal analysis (lead); Investigation (lead); Methodology (supporting); Software (equal); Validation (lead); Writing – original draft (lead); Writing – review & editing (supporting). **Sabuhi Badalov**: Investigation (supporting); Methodology (supporting); Validation (supporting); Writing – review & editing (supporting). **Achim Wixforth**: Conceptualization (supporting); Funding acquisition (equal); Writing – review & editing (supporting). **Dirk Volkmer**: Conceptualization (supporting); Formal analysis (supporting); Funding acquisition (equal); Investigation (supporting); Methodology (supporting); Supervision (supporting); Writing – original draft (supporting); Writing – review & editing (supporting). **Harald Oberhofer**: Conceptualization (lead); Data curation (equal); Funding acquisition (equal); Methodology (lead); Resources (lead); Software (equal); Supervision (lead); Writing – original draft (supporting); Writing – review & editing (lead).

## DATA AVAILABILITY

The data supporting the findings of this study are openly available at the Zenodo archive under DOI: 10.5281/zenodo.15577626.

## REFERENCES


[1] H. Furukawa, K. E. Cordova, M. O'Keeffe, and O. M. Yaghi, "The chemistry and applications of metal-organic frameworks," Science **341**, 1230444 (2013).

[2] S. Kitagawa *et al.*, "Metal–organic frameworks (MOFs)," Chem. Soc. Rev. **43**, 5415–5418 (2014).

[3] L. E. Kreno, K. Leong, O. K. Farha, M. Allendorf, R. P. Van Duyne, and J. T. Hupp, "Metal–organic framework materials as chemical sensors," Chem. Rev. **112**, 1105–1125 (2012).

[4] C. Muschielok, A. Reiner, R. Röß-Ohlenroth, A. Kalytta-Mewes, D. Volkmer, A. Wixforth, and H. Oberhofer, "Combining theory and experiments to study the influence of gas sorption on the conductivity properties of metal–organic frameworks," ACS Appl. Mater. Interfaces **14**, 33662–33674 (2022).

[5] M. Eddaoudi, J. Kim, N. Rosi, D. Vodak, J. Wachter, M. O'Keeffe, and O. M. Yaghi, "Systematic design of pore size and functionality in isoreticular mofs and their application in methane storage," Science **295**, 469–472 (2002).

[6] L. J. Murray, M. Dincă, and J. R. Long, "Hydrogen storage in metal–organic frameworks," Chem. Soc. Rev. **38**, 1294–1314 (2009).

[7] J. Liu, L. Chen, H. Cui, J. Zhang, L. Zhang, and C.-Y. Su, "Applications of metal–organic frameworks in heterogeneous supramolecular catalysis," Chem. Soc. Rev. **43**, 6011–6061 (2014).

[8] V. Pascanu, G. González Miera, A. K. Inge, and B. Martín-Matute, "Metal–organic frameworks as catalysts for organic synthesis: A critical perspective," J. Am. Chem. Soc. **141**, 7223–7234 (2019).

[9] S. Horike, D. Umeyama, and S. Kitagawa, "Ion conductivity and transport by porous coordination polymers and metal–organic frameworks," Acc. Chem. Res. **46**, 2376–2384 (2013).

[10] L. Sun, M. G. Campbell, and M. Dincă, "Electrically conductive porous metal–organic frameworks," Angew. Chem., Int. Ed. **55**, 3566–3579 (2016).

[11] C. Muschielok and H. Oberhofer, "Aspects of semiconductivity in soft, porous metal-organic framework crystals," J. Chem. Phys. **151**, 015102 (2019).

[12] L. S. Xie, G. Skorupskii, and M. Dinca, "Electrically conductive metal–organic frameworks," Chem. Rev. **120**, 8536–8580 (2020).

[13] S. Namsani and A. O. Yazaydin, "Electric field induced rotation of halogenated organic linkers in isoreticular metal–organic frameworks for nanofluidic applications," Mol. Syst. Des. Eng. **3**, 951–958 (2018).

[14] J. Perego, C. X. Bezuidenhout, S. Bracco, S. Piva, G. Prando, C. Aloisi, P. Carretta, J. Kaleta, T. P. Le, P. Sozzani, A. Daolio, and A. Comotti, "Benchmark dynamics of dipolar molecular rotors in fluorinated metal-organic frameworks," Angew. Chem., Int. Ed. **62**, e202215893 (2023).

[15] Y.-S. Su, E. S. Lamb, I. Liepuoniute, A. Chronister, A. L. Stanton, P. Guzman, S. Pérez-Estrada, T. Y. Chang, K. N. Houk, M. A. Garcia-Garibay, and S. E. Brown, "Dipolar order in an amphidynamic crystalline metal–organic framework through reorienting linkers," Nat. Chem. **13**, 278–283 (2021).

[16] J. Schnabel, A. Schulz, P. Lunkenheimer, and D. Volkmer, "Benzothiadiazole-based rotation and possible antipolar order in carboxylate-based metal-organic frameworks," Commun. Chem. **6**, 161 (2023).

[17] R. Freund, A. Schulz, P. Lunkenheimer, M. Kraft, T. Bergler, H. Oberhofer, and D. Volkmer, "Exploring dipolar dynamics and ionic transport in metal-organic frameworks: Experimental and theoretical insights," Adv. Funct. Mater. **2024**, 2415376.

[18] P. V. Alekseevskiy, S. Rzhevskiy, V. Gilemkhanova, N. K. Kulachenkov, A. Sapianik, M. Barsukova, V. P. Fedin, and V. A. Milichko, "Flexible metal-organic framework for mechanical sub tbyte inch$^{-2}$ data recording under ambient condition," Adv. Mater. Interfaces **8**, 2101196 (2021).

[19] H. Lian, X. Cheng, H. Hao, J. Han, M.-T. Lau, Z. Li, Z. Zhou, Q. Dong, and W.-Y. Wong, "Metal-containing organic compounds for memory and data storage applications," Chem. Soc. Rev. **51**, 1926–1982 (2022).

[20] J. Xiao, H. Li, W. Zhao, C. Cai, T. You, Z. Wang, M. Wang, F. Zeng, J. Cheng, J. Li, and X. Duan, "Zinc-metal–organic frameworks with tunable UV diffuse-reflectance as sunscreens," J. Nanobiotechnol. **20**, 87 (2022).

[21] S. Ullah and T. Thonhauser, "Flexible MOFs as pressure-tunable filters for hydrocarbon separation," J. Phys. Chem. C **128**, 15542–15548 (2024).

[22] N. C. Burtch, A. Torres-Knoop, G. S. Foo, J. Leisen, C. Sievers, B. Ensing, D. Dubbeldam, and K. S. Walton, "Understanding DABCO nanorotor dynamics in isostructural metal–organic frameworks," J. Phys. Chem. Lett. **6**, 812–816 (2015).

[23] P. Martinez-Bulit, A. J. Stirk, and S. J. Loeb, "Rotors, motors, and machines inside metal–organic frameworks," Trends Chem. **1**, 588–600 (2019).

[24] G. Prando, J. Perego, M. Negroni, M. Riccò, S. Bracco, A. Comotti, P. Sozzani, and P. Carretta, "Molecular rotors in a metal–organic framework: Muons on a hyper-fast carousel," Nano Lett. **20**, 7613–7618 (2020).

[25] G. Nascimbeni, C. Wöll, and E. Zojer, "Electrostatic design of polar metal–organic framework thin films," Nanomaterials **10**, 2420 (2020).

[26] J. Valasek, "Piezo-electric and allied phenomena in rochelle salt," Phys. Rev. **17**, 475–481 (1921).

[27] W. Zhang and R.-G. Xiong, "Ferroelectric metal–organic frameworks," Chem. Rev. **112**, 1163–1195 (2012).

[28] K. Asadi and M. A. van der Veen, "Ferroelectricity in metal–organic frameworks: Characterization and mechanisms," Eur. J. Inorg. Chem. **2016**, 4332–4344.

[29] H. Xiang, B. Xu, Y. Xia, J. Yin, and Z. Liu, "Piezoelectricity in two-dimensional covalent organic frameworks," J. Appl. Phys. **121**, 225112 (2017).

[30] Q. Gu, X. Lu, C. Chen, X. Wang, F. Kang, Y. Y. Li, Q. Xu, J. Lu, Y. Han, W. Qin, and Q. Zhang, "High-performance piezoelectric two-dimensional covalent organic frameworks," Angew. Chem. Int. Ed. **63**, e202409708 (2024).

[31] Q. Gu, X. Lu, W. Qin, and Q. Zhang, "2D piezoelectric covalent organic frameworks: Construction, characterization, and potential applications," ChemPhysChem **26**, e202500148 (2025).

[32] L. Guan, D. Mehdi, H. Li, F. Chen, and S. Jin, "Covalent organic frameworks: An emerging class of piezoelectric materials for mechanical energy transfer application," Chin. Chem. Lett. **2025**, 111389.

[33] Z. Li, Z. Dong, Z. Zhang, B. Wei, C. Meng, W. Zhai, Y. Wang, X. Cao, B. Han, and Y. Liu, "Covalent organic frameworks for boosting $H_2O_2$ photosynthesis via the synergy of multiple charge transfer channels and polarized field," Angew. Chem. **137**, e202420218 (2025).

[34] Y. Zhang, Y. Peng, X. Li, H. Lu, and Z. Ma, "Piezo-photocatalytic synergy in COF/PVDF-HFP porous films for efficient dye degradation and broad-spectrum antibacterial," Mater. Today (submitted) (2025), available at SSRN: https://ssrn.com/abstract=5508608.

[35] A. Comotti, S. Bracco, and P. Sozzani, "Molecular rotors built in porous materials," Acc. Chem. Res. **49**, 1701–1710 (2016).

[36] J. Dong, V. Wee, S. B. Peh, and D. Zhao, "Molecular-rotor-driven advanced porous materials," Angew. Chem. Int. Ed. **60**, 16279–16292 (2021).

[37] L. Feng, R. D. Astumian, and J. F. Stoddart, "Controlling dynamics in extended molecular frameworks," Nat. Rev. Chem **6**, 705–725 (2022).

[38]G.-C. Xu, X.-M. Ma, L. Zhang, Z.-M. Wang, and S. Gao, "Disorder–Order ferroelectric transition in the metal formate framework of $[NH_4]$ $[Zn(HCOO)_3]$," J. Am. Chem. Soc. **132**, 9588–9590 (2010).
[39]A. Hjorth Larsen, J. Jørgen Mortensen, J. Blomqvist, I. E. Castelli, R. Christensen, M. Dułak, J. Friis, M. N. Groves, B. Hammer, C. Hargus, E. D. Hermes, P. C. Jennings, P. Bjerre Jensen, J. Kermode, J. R. Kitchin, E. Leonhard Kolsbjerg, J. Kubal, K. Kaasbjerg, S. Lysgaard, J. Bergmann Maronsson, T. Maxson, T. Olsen, L. Pastewka, A. Peterson, C. Rostgaard, J. Schiøtz, O. Schütt, M. Strange, K. S. Thygesen, T. Vegge, L. Vilhelmsen, M. Walter, Z. Zeng, and K. W. Jacobsen, "The atomic simulation environment—A Python library for working with atoms," J. Phys. Condens. Matter **29**, 273002 (2017).
[40]A. P. Thompson, H. M. Aktulga, R. Berger, D. S. Bolintineanu, W. M. Brown, P. S. Crozier, P. J. in 't Veld, A. Kohlmeyer, S. G. Moore, T. D. Nguyen, R. Shan, M. J. Stevens, J. Tranchida, C. Trott, and S. J. Plimpton, "Lammps—A flexible simulation tool for particle-based materials modeling at the atomic, meso, and continuum scales," Comput. Phys. Commun. **271**, 108171 (2022).
[41]T. D. Kühne, M. Iannuzzi, M. Del Ben, V. V. Rybkin, P. Seewald, F. Stein, T. Laino, R. Z. Khaliullin, O. Schütt, F. Schiffmann, D. Golze, J. Wilhelm, S. Chulkov, M. H. Bani-Hashemian, V. Weber, U. Borštnik, M. Taillefumier, A. S. Jakobovits, A. Lazzaro, H. Pabst, T. Müller, R. Schade, M. Guidon, S. Andermatt, N. Holmberg, G. K. Schenter, A. Hehn, A. Bussy, F. Belleflamme, G. Tabacchi, A. Glöß, M. Lass, I. Bethune, C. J. Mundy, C. Plessl, M. Watkins, J. VandeVondele, M. Krack, and J. Hutter, "CP2K: An electronic structure and molecular dynamics software package—Quickstep: Efficient and accurate electronic structure calculations," J. Chem. Phys. **152**, 194103 (2020).
[42]P. G. Boyd, S. M. Moosavi, M. Witman, and B. Smit, "Force-field prediction of materials properties in metal-organic frameworks," J. Phys. Chem. Lett. **8**, 357–363 (2017).
[43]P. G. Boyd, S. M. Moosavi, M. Witman, and B. Smit (2025). "Github-peteboyd/lammps_interface: Automatic generation of lammps input files for molecular dynamics simulations of MOFs," GitHub. https://github.com/peteboyd/lammps_interface
[44]G. Kresse and J. Hafner, "*Ab initio* molecular dynamics for open-shell transition metals," Phys. Rev. B **48**, 13115–13118 (1993).
[45]G. Kresse and J. Furthmüller, "Efficient iterative schemes for *ab initio* total-energy calculations using a plane-wave basis set," Phys. Rev. B **54**, 11169–11186 (1996).
[46]G. Kresse and D. Joubert, "From ultrasoft pseudopotentials to the projector augmented-wave method," Phys. Rev. B **59**, 1758–1775 (1999).
[47]S. Grimme, S. Ehrlich, and L. Goerigk, "Effect of the damping function in dispersion corrected density functional theory," J. Comput. Chem. **32**, 1456–1465 (2011).
[48]J. Heyd, G. E. Scuseria, and M. Ernzerhof, "Erratum: "hybrid functionals based on a screened Coulomb potential" [J. Chem. Phys. 118, 8207 (2003)]," J. Chem. Phys. **124**, 219906 (2006).
[49]M. R. Ams, N. Trapp, A. Schwab, J. V. Milić, and F. Diederich, "Chalcogen bonding '2S–2N Squares' versus competing interactions: Exploring the recognition properties of sulfur," Chem.–Eur. J. **25**, 323–333 (2019).
[50]F. Neese, "The orca program system," WIREs Comput. Mol. Sci. **2**, 73–78 (2012).
[51]S. Grimme, C. Bannwarth, and P. Shushkov, "A robust and accurate tight-binding quantum chemical method for structures, vibrational frequencies, and noncovalent interactions of large molecular systems parametrized for all spd-Block elements ($Z$ = 1–86)," J. Chem. Theory Comput. **13**, 1989–2009 (2017).
[52]S. Ehlert, S. Grimme, and A. Hansen, "Conformational energy benchmark for longer *n*-alkane chains," J. Phys. Chem. A **126**, 3521–3535 (2022).
[53]C. Bannwarth, E. Caldeweyher, S. Ehlert, A. Hansen, P. Pracht, J. Seibert, S. Spicher, and S. Grimme, "Extended tight–binding quantum chemistry methods," WIREs Comput. Mol. Sci. **11**, e1493 (2021).